

# A DIGITAL ARCHIVE OF HI 21 CM LINE SPECTRA OF OPTICALLY-TARGETED GALAXIES

CHRISTOPHER M. SPRINGOB<sup>1</sup>, MARTHA P. HAYNES<sup>1,2</sup>, RICCARDO GIOVANELLI<sup>1,2</sup>, AND BRIAN R. KENT<sup>1</sup>

*Draft version October 30, 2018*

## ABSTRACT

We present a homogeneous compilation of HI spectral parameters extracted from global 21 cm line spectra for some 9000 galaxies in the local universe (heliocentric velocity  $-200 < V_{\odot} < 28,000$  km s<sup>-1</sup>) obtained with a variety of large single dish radio telescopes but reanalyzed using a single set of parameter extraction algorithms. Corrections to the observed HI line flux for source extent and pointing offsets and to the HI line widths for instrumental broadening and smoothing are applied according to model estimates to produce a homogenous catalog of derived properties with quantitative error estimates. Where the redshift is available from optical studies, we also provide flux measurements for an additional 156 galaxies classified as marginal HI detections and rms noise limits for 494 galaxies classified as nondetections. Given the diverse nature of the observing programs contributing to it, the characteristics of the combined dataset are heterogeneous, and as such, the compilation is neither integrated HI line flux nor peak flux limited. However, because of the large statistical base and homogenous reprocessing, the spectra and spectral parameters of galaxies in this optically targeted sample can be used to complement data obtained at other wavelengths to characterize the properties of galaxies in the local universe and to explore the large scale structures in which they reside.

*Subject headings:* galaxies: distances and redshifts — galaxies: fundamental parameters — radio lines: galaxies — techniques: spectroscopic — astronomical data bases: miscellaneous

## 1. INTRODUCTION

Neutral hydrogen constitutes a significant component of the interstellar medium of disk galaxies. The study of its abundance and kinematics, as measured by the 21 cm emission line, has seen applications to a variety of astrophysical problems, ranging from studies of the large scale distribution of galaxies to secular evolution in clusters. HI line emission carries information about the distribution of neutral gas, and through tracing of its velocity field, of the total mass in a galaxy. Even in the absence of any spatial information about the distribution of the gas, the global HI line profile, contained within the beam of a single dish telescope or integrated over the entire HI distribution where resolved, provides three key indicators: (1) the observed redshift of the system as a whole; (2) the observed HI line flux, which, in the optically thin case, can be related to the HI mass; and (3) the observed HI line full width, which, when corrected to face-on viewing, is related to the total rotational velocity of the HI gas. These quantities have been used for diverse applications such as the tracing of large scale structure by gas-rich systems, the comparative HI content of galaxies in differing environments and the derivation of secondary distances using the Tully-Fisher method (Tully & Fisher 1977).

HI line systemic velocities, fluxes and characteristic velocity widths have been recorded for more than 20,000 galaxies and presented in large published compilations such as that of Huchtmeier & Richter (1991) and the

*Third Reference Catalog of Bright Galaxies* (RC3, de Vaucouleurs *et al.* 1991). Until recently, the vast majority of extragalactic HI line spectral parameters were associated with observational targets selected from optical catalogs. Only recently have large-area HI blind surveys been undertaken, notably the Arecibo HI Strip Survey (AHISS; Zwaan *et al.* 1997), the Arecibo Dual Beam Survey (ADBS; Rosenberg & Schneider 2000), the HI Jodrell All-Sky Survey (HIJASS; Lang *et al.* 2003) and the HI Parkes All-Sky Survey (HIPASS; Barnes *et al.* 2001; Koribalski *et al.* 2004; Meyer *et al.* 2004). Most recently, the blind HI survey conducted with the Parkes Telescope multifield array (HIPASS) has catalogued 4315 extragalactic HI line sources (HIPASS catalog; Meyer *et al.* 2004) south of Dec.  $< +2^{\circ}$  identified purely on the peak flux of their HI line emission profiles. Perhaps surprisingly, extremely few systems detected in the HI blind surveys have no optical counterpart (Kilborn *et al.* 2000; Rosenberg & Schneider 2002), but understanding the difference between optical- and HI-selected samples is critical to determining the true census of gas-bearing objects in the nearby universe and the relationship of present day disks to the damped Lyman  $\alpha$  absorbers seen in QSO spectra.

With the exception of the HIPASS dataset which has been processed uniformly and can be accessed digitally through a public website (<http://hipass.aus-vo.org/>), a significant disadvantage of past compilations arises from heterogenous processing and parameter extraction algorithms, as well as the lack of availability of the digital spectra themselves. In many cases, error or noise estimates are lacking and corrections for instrumental effects not applied or derivable. Because of our own on-going work related to the applications of HI spectral data in correlative and secondary studies, we have developed and maintained a digital archive of HI line spectra for some 9000 optically-selected galaxies observed by us and our

<sup>1</sup> Center for Radiophysics and Space Research, Cornell University, Space Sciences Building, Ithaca, NY 14853; springob@astro.cornell.edu, haynes@astro.cornell.edu, riccardo@astro.cornell.edu, bkent@astro.cornell.edu

<sup>2</sup> National Astronomy and Ionosphere Center, Cornell University, Ithaca, NY 14853. The National Astronomy and Ionosphere Center is operated by Cornell University under a cooperative agreement with the National Science Foundation.

numerous collaborators using various telescopes over the last 20+ years. Two of the telescopes used, the 91 m and 42 m telescopes of the National Radio Astronomy Observatory<sup>3</sup> at Green Bank, are no longer operational (in fact, the 91 m telescope no longer exists). While HI parameters for most of these datasets have been presented previously, changing scientific objectives and computer capabilities have led to advances in the robustness of parameter extraction algorithms. In order to establish a well-characterized and permanent digital archive of these global HI profiles, we have reanalyzed the global HI line profiles using a single set of processing and parameter estimation algorithms. In this paper, we present a homogeneous compilation of the extracted HI line parameters and provide quantitative corrections and error estimates. These data are being used in a variety of ongoing studies, including a robust estimation of the HI mass function (Springob, Haynes, & Giovanelli 2005) and studies of the local peculiar velocity field.

In Section 2, we review the observational circumstances of the archival dataset as well as present new HI observations undertaken with the Arecibo 305 meter telescope. Section 3 discusses the process of extracting useful parameters from the global HI line profiles and the corrections required to derive physically meaningful quantities. The archive is presented in Section 4, followed by discussion of the characteristics of the data set, its completeness and its limitations in Section 5. A brief summary concludes in Section 6.

## 2. OBSERVATIONS

The majority of the HI line datasets included in the current compilation have been discussed in previous publications. Here we review the general characteristics of the telescopes employed to conduct the observations, summarized in Table 1, and also present the results of new observations for a sample of 145 obtained with the upgraded Arecibo telescope.

### 2.1. Archival Datasets

Since the early 1980’s, we have attempted to maintain a digital archive of the extragalactic HI global profiles we and our collaborators have observed at a number of large single-dish radiotelescopes, namely the 305 m Arecibo telescope of the National Astronomy and Ionosphere Center, the late 91 m and 42 m Green Bank telescopes of the National Radio Astronomy Observatory, the Nançay radio telescope of the Observatory of Paris and the Effelsberg 100 m telescope of the Max Planck Institut für Radioastronomie. The basic parameters of those telescopes are summarized in Table 1, along with a compilation of the principal references to the published works which include discussions of the individual observing programs, observational setups and target selection criteria. Observations at Arecibo employed several different L-band feed systems, denoted by their designated names: one of the high gain dual circular polarization feeds (“dual circular”; two such similar feeds were available, one of which was remotely tunable in frequency) and a low sidelobe linear polarization L-band feed (“flat”

feed). During the 1990’s, the Arecibo telescope was upgraded and a low noise, broadband secondary and tertiary reflector Gregorian optical system was installed; observations made with it are described in the following subsection. Nearly all observations were conducted in total power mode, with a position switching technique used to remove instrumental baseline effects. At each telescope, calibration of the noise diodes was performed by conducting observations of continuum sources from the catalog of Bridle *et al.* (1972), and both the flux and velocity scales were further checked by observations of a sample of strong HI line emitting galaxies. Typical on-source integration times were dictated by signal-to-noise requirements and varied from as little as 5 minutes at Arecibo to as much as 2 hours with the 42 m and Nançay telescopes. Final spectra are the accumulated weighted averages of multiple ON-OFF pairs.

The main distinctions among the HI datasets arise from differences in the sensitivities achieved with the different telescopes, and differences in the resolution and bandwidth associated with the available spectral backends. In order both to permit the analysis of instrumental effects and to measure widths using the same algorithm, the accumulated and calibrated final spectra were exported from the respective on-line data format into the standard ANALYZ-GALPAC “history file” format developed by RG at the Arecibo Observatory and were thus available in digital form for reprocessing using the algorithms described below. All accumulated spectra have been re-smoothed and re-baselined using an interactive process that allows the user to select the degree of smoothing (typically Hanning, but sometimes also a 3 channel BOXCAR in order to improve signal-to-noise, as noted in Table 3), choose the baseline regions and order (typically 3), flag the boundaries for flux integration and examine the results before they are stored away in the permanent archive.

All spectra presented here have been reprocessed using the same parameter extraction algorithms, producing new measurements which supercede those presented previously.

### 2.2. New Arecibo Observations

In addition to the HI spectra already contained in the digital archive, new HI line observations were conducted with the Arecibo 305 meter telescope and its Gregorian optics system between September and November 2001. 116 galaxies were detected, and an additional 29 galaxies for which we have optical heliocentric velocities yielded upper limits. Targets were selected from among inclined spirals included in our private database, referred to as the Arecibo General Catalog (AGC). The new observations preferentially targeted those objects which appeared to be good Tully-Fisher candidates and for which we did not already have HI spectral parameters, in the region of the Pisces-Perseus supercluster, that is  $22^h < \text{R.A.} < 4^h$ ,  $0^\circ < \text{Dec.} < +38^\circ$ .

The L-band narrow receiver was used in 9-level sampling mode for all observations, feeding each polarization to four correlator boards with 1024 channels and 25 MHz bandwidth (yielding a velocity resolution of 5.15 km s<sup>-1</sup>). In most (but not all) cases, the redshift was not known in advance so that a search mode was employed, staggering the four boards to cover a total of 85

<sup>3</sup> The National Radio Astronomy Observatory is operated by Associated Universities, Inc. under a cooperative agreement with the National Science Foundation.

TABLE 1  
CHARACTERISTICS OF SINGLE DISH TELESCOPES AND THEIR DATASETS

Telescope/Feed	Aperture (m)	Gain (KJy <sup>-1</sup> )	HPBW ( $^{\circ}$ )	# spectra	Original Reference
Arecibo “dual circular”	305	8.0	3.3	6475	HG84,a,b,c,d,e,f,g,h,k,m,n,o,p,q,s
Arecibo “flat”	305	6.0	3.9	20	HHG,o,q
Arecibo “Gregorian”	305	11.0	3.5	116	this work
Effelsberg	100	1.5	8.8	66	m
Green Bank 91 m	91	1.1	10.0	1090	i,j,m,n,o
Green Bank 42 m	42	0.25	21.0	706	l,m,r
Nançay	300×34.6	1.2	4×20	377	m

<sup>a</sup>Freudling *et al.* 1988

<sup>b</sup>Freudling *et al.* 1992

<sup>c</sup>Giovanelli *et al.* 1986

<sup>d</sup>Giovanelli & Haynes 1989

<sup>e</sup>Giovanelli & Haynes 1993

<sup>f</sup>Giovanelli *et al.* 1997

<sup>g</sup>Haynes & Giovanelli 1986

<sup>h</sup>Haynes & Giovanelli 1991a

<sup>i</sup>Haynes & Giovanelli 1991b

<sup>j</sup>Haynes *et al.* 1988

<sup>k</sup>Haynes *et al.* 1997

<sup>l</sup>Haynes *et al.* 1998

<sup>m</sup>Haynes *et al.* 1999

<sup>n</sup>Magri *et al.* 1988

<sup>o</sup>Magri 1994

<sup>p</sup>Scodreggio *et al.* 1995

<sup>q</sup>van Zee *et al.* 1995

<sup>r</sup>van Zee *et al.* 1997

<sup>s</sup>Wegner *et al.* 1993

MHz bandwidth. The first board was centered at the 21 cm line rest frequency of 1420.40578 MHz, while the other three boards overlapped but with center frequencies offset at 20, 40, and 60 MHz below this frequency. On all nights, the system temperature was approximately 30 K. All observations were conducted in a total power, position switching mode as a sequence of ON–source and OFF–source pairs of 4 minutes each. The final spectrum is the average of the combination of the successive ON–OFF pairs. The total number of ON/OFF observations made for each galaxy varied based on the signal-to-noise ratio, and ranged from one to four. On the first three nights of observations, each board was Doppler corrected to heliocentric velocity at the start of each ON–OFF pair. Beginning with the fourth night, the same Doppler correction was applied to each of the four boards, allowing the spacing between correlators to remain at 20 MHz exactly. Beginning on the fifth night, we used the NAIC “radar blanker”, which detects the San Juan airport’s radar and suspends data-taking for brief intervals around the pulse arrival times, for all observations in which the redshift of the galaxy was either not known a priori or known to be such that the redshifted 1420 MHz HI line would overlap with the 1350 MHz frequency of the airport radar.

Whereas data reduction for all other Arecibo observations presented here was performed using the Arecibo ANALYZ–GALPAC analysis system, the data reduction for these new observations was carried out using the AIPS++ software package <sup>4</sup>. The reduction algorithms

<sup>4</sup> The AIPS++ (Astronomical Information Processing System) is a product of the AIPS++ Consortium. AIPS++ is available for use under the Gnu Public License. Further information may be

match those carried out for the earlier observations in ANALYZ–GALPAC (and discussed in Haynes *et al.* 1999 and references therein) exactly, with one exception. We have used the ‘setfreqmed’ and ‘settimemed’ functions within the AIPS++ ‘autoflag’ package to eliminate individual time-frequency pixels found to be corrupted by radio frequency interference (RFI). The RFI identification algorithm flags pixels that deviate by more than 10 times the median deviation from a sliding median of width 10 pixels in both the time and frequency dimensions. The width of each pixel in the time domain is 1 second.

### 3. HI 21 CM LINE FLUXES, SYSTEMIC VELOCITIES AND LINE WIDTHS

The parameters extracted from global 21 cm line profiles obtained with single dish telescope require correction before physical quantities can be derived from them. Here the process for conversion from observed to corrected parameters is described in some detail.

#### 3.1. Integrated Line Fluxes

Modern radio telescopes can be continuum flux calibrated to a small fraction of their system noise, but as discussed by van Zee *et al.* (1997), the accuracy with which HI line fluxes can be measured is much less precise. Beyond the continuum flux calibration which can be achieved at the better than 2% level, the accuracy with which line fluxes can be measured depends both on baseline stability and on corrections that must be applied to the observed values. The HI line fluxes  $S_{obs} = \int S(V) dV$  presented here have been measured on the smoothed and

obtained from <http://aips2.nrao.edu>.

baseline subtracted profiles by an interactive process in which the user marks the range of correlator channels over which the flux is measured by integrating the emission within these boundaries. The observed line flux  $S_{obs}$  must then be corrected for (1) beam attenuation, (2) pointing offsets, and (3) HI self absorption. We discuss each correction separately.

Since the HI distribution in a galaxy is often partially resolved by the telescope beam, the HI line flux detected by a given telescope underestimates the true flux by an amount that depends on how much the source HI distribution fills, or overfills, the beam. Since the HI distribution is generally not known, an estimate of the beam attenuation correction is based on the adoption of a model HI distribution and an average telescope beam power pattern. The power patterns of the Arecibo, 42 m, 91 m and 100 m telescopes are assumed to be Gaussians with half power beam width (HPBW) as given in Table 1. For the Nançay telescope, the beam width is assumed to be a two-dimensional Gaussian with HPBW of  $4'$  in the R.A. direction and  $20'$  in the Dec. direction. The HI distribution is modeled as the sum of two Gaussians, one of negative amplitude to produce a central hole (Shostak 1978; Hewitt, Haynes & Giovanelli 1983, hereafter HHG). Following Section IV of HHG, the HI surface brightness distribution  $\sigma_H(r)$  is assumed to be characterized by the same axial ratio and to lie along the same position angle as the optical galaxy and is scaled such that  $D_{70}$ , the diameter encompassing 70% of the HI mass, equals  $1.3 a$ , where  $a$  is the optical major axis, in arcminutes, taken from either the Uppsala General Catalog (Nilson 1973, hereafter UGC) or the ESO-Uppsala Survey of the ESO(B) Atlas (Lauberts 1982, hereafter ESO), or estimated by us on the POSS-I<sup>5</sup>. Following HHG, the fraction  $f_1$  of the source flux that is detected by the telescope beam is given by

$$f_1 = \frac{\sum_{j=1,2} \left[ \frac{a_j \theta_j^2}{(1+\theta_j^2/\theta_B^2)^{1/2} (1+\theta_j^2 \cos^2 i / \theta_B^2)^{1/2}} \right]}{\sum_{j=1,2} a_j \theta_j^2} \quad (1)$$

Like HHG, we assume a double Gaussian  $\sigma_H$  of amplitude  $a_2 = -0.6a_1$  and relative extent  $\theta_2 = 0.23\theta_1$ . Note that  $\theta_B$  above is not the HPBW but rather the beam extent at which the power pattern falls by  $e^{-1}$ , assuming a Gaussian response. The inclination  $i$  of the galaxy is derived from the observed optical axial ratio  $b/a$  and an assumed intrinsic axial ratio that varies from 0.10 for the latest spirals to 0.23 for the earliest following Section IV.e of Haynes & Giovanelli (1984; HG84).

The correction factor  $c_1$  that accounts for beam attenuation is the inverse of this fraction,  $c_1 = 1/f_1 > 1$  and approaches 1 when the HI distribution is significantly smaller than the telescope beam. Because the HI extent of HI-normal spirals is significantly larger than their optical dimension, the application of this correction is very important for most HI observations conducted at Arecibo with its relatively small HPBW ( $\sim 3.5'$ ). For example, face-on galaxies with optical sizes equal to about half the HPBW (i.e.,  $a \sim 1.7'$ ) have corrections of about 25%;

a similar edge-on HI disk requires a correction half as large. For an object inclined by  $\sim 45^\circ$  and an optical extent equal to the HPBW, the correction amounts to  $\sim 60\%$ . Because the HI disk can normally be traced well beyond the optical extent, the observed HI line flux in face-on systems as small as  $0.8'$  require corrections of 5% or more. The other telescopes that have been employed have substantially wider beams, and there are few galaxies observed with them for which this correction is significant.

Additionally, if the source HI distribution is not centered in the telescope beam,  $S_{obs}$  will be less than it would be in the absence of such pointing offset. Departures from centering arise both from the intrinsic accuracy of a radio telescope to center on the input coordinates and from errors in the target coordinates relative to the true source position, and they are important only when such offsets subtend a substantial fraction of the beam extent. For older observations conducted with the Arecibo line feeds, the rms pointing accuracy of the telescope system was  $\sim 15''$  in both R.A. and Dec. The precise amplitude of this error is not known but has been assumed to be random and of order 5% (HG84). Therefore, all HI lines fluxes derived from spectra obtained at Arecibo prior to 1993 have been multiplied by a constant factor of  $c_2 = 1.05$  to account for this systematic bias. This correction is not applied to other datasets.

Similarly, older datasets are also affected by the inaccuracy of the coordinates input to position the telescope on source at the time the observations were conducted. In such cases, the flux is also underestimated by an amount which depends on the ratio of the angular displacement of the center of the telescope beam from the true source location to the beam extent and is important for some of the older Arecibo line feed data. For spectra in our digital archive, a measure of the amount by which the flux has been underestimated because of coordinate inaccuracy can be calculated because the input coordinates are recorded in the digital spectra. To estimate this correction factor, we have performed a set of numerical simulations mimicking observations offset from the Arecibo line feed beam center, by convolving the beam power pattern with template galaxy HI distributions following the method developed in HHG. These simulations confirm that the measured flux in the simulations is relatively insensitive to the position angle of the galaxy (assumed to follow the optical image), but quite sensitive to the angular displacement of the beam center from the center of the HI disk. Following again HHG's result that  $D_{70} = 1.3a$ , we relate the angular displacement  $\Theta$  of the targeted position from the true position and the optical apparent diameter  $a$  to the flux correction  $c_3$ , as shown in Figure 1. For each galaxy observed with the Arecibo line feeds for which the pointing offset exceeds  $0.1'$ , we adopt the flux correction associated with the closest match in both optical size and pointing offset shown in Figure 1. The figure illustrates the point that the required flux correction can be very large even for optically small galaxies, if the pointing offset is large. However, there are only 183 galaxies for which this correction boosts the flux by a factor of  $c_3 = 1.5-2.0$ , and only 62 for which the flux correction is more than a factor of  $c_3 = 2$ .

Lastly, optical depth effects also can result in a decrease of detected HI line flux if not all the photons

<sup>5</sup> The National Geographic Society - Palomar Observatory Sky Atlas (POSS-I) was made by the California Institute of Technology with grants from the National Geographic Society.

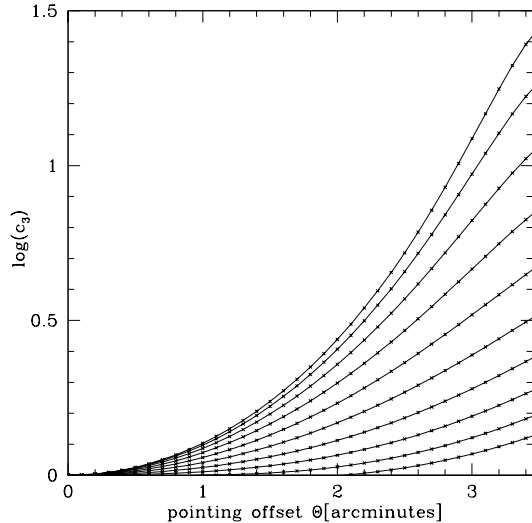


FIG. 1.— Simulated pointing offset flux correction  $c_3$  for older AO line feed observations for galaxies of different optical sizes. The flux correction is the ratio of a galaxy’s actual flux to its observed flux given its size and the offset of the commanded telescope position during the observations from the optical galaxy center. The ten different curves represent corrections for different optical sizes. The top curve is for galaxies with an optical major diameter of  $0.54'$ . The next curve for  $1.08'$ , and so forth, down to  $5.4'$ . The average pointing offset for all Arecibo observations is  $\sim 0.21'$  so that the application of this correction is significant only in a relatively small number of cases.

escape. In the denser regions of disks, the interstellar medium can be optically thick at 21 cm (Braun 1997), but the filling factor of opaque regions is small in the vast majority of disks. Following Giovanelli *et al.* (1994) and using the optical axial ratio as the measure of disk inclination, we correct for HI self-absorption by multiplying the measured HI line fluxes by the factor  $c_4 = (a/b)^{0.12}$ . This effect is small, with less than 30% of the HI line flux self absorbed in the most highly inclined systems. However, there are some galaxies for which this is the dominant correction. Because this correction is model-dependent, and the interested reader may wish to apply a different self-absorption correction, we report the self-absorption corrected flux separately.

The two values we report for the corrected HI line flux are then  $S_c = c_1 c_2 c_3 S_{obs}$ , including the corrections for source extent and pointing, and  $S_c^{abs} = c_1 c_2 c_3 c_4 S_{obs}$ , which also includes the correction for HI self-absorption.  $S_c^{abs}$  is, on average, 25% larger than the observed line flux. It should be noted that all of the corrections increase the value of line flux used in the calculation of HI masses. Comparison of values presented here with others in the literature should take into account similar treatments in order to avoid systematic differences in the derived HI masses which might otherwise be interpreted as physical differences.

### 3.1.1. Integrated Line Flux Errors

Several different sources of error affect the measurement of integrated HI line fluxes. The first is the uncertainty in the absolute flux calibration commonly achieved by firing a noise diode at regular intervals (van Zee *et al.* 1997) and understanding well the telescope gain and

its variation. Because modern telescope systems are significantly more stable than older ones, we follow van Zee *et al.* (1997) in estimating that the uncertainty introduced by the noise diode calibration is 2% of the observed integrated flux for those observations made with the 42 m Green Bank telescope and for those made with the Arecibo telescope after the installation of its Gregorian optical system. For all other observations, we estimate the uncertainty introduced by the noise diode calibration to be 10% of the observed integrated flux. Further, we estimate that the uncertainty introduced by the correction coefficients is  $(c_1 c_2 c_3 c_4 - 1) S_{obs} / 3$ .

The integrated flux error contribution from *statistical* uncertainty has been discussed by both Fouqué *et al.* (1990b) and Schneider *et al.* (1990), both of whom derive analytical expressions for the statistical uncertainty. Unlike the Fouqué *et al.* (1990b) formula, however, the Schneider *et al.* (1990) formula does not include any assumptions regarding the shape of the line profile, but *does* include the contribution to the total error stemming from uncertainties in the baseline fit. We therefore adopt the Schneider *et al.* (1990) formula, with one modification. The formula includes a dependence on  $W_{P20}$ , the line width measured at 20% of the peak flux density. We have our own preferred width measurement algorithm which is explained in Section 3.2. Because we find that the value of  $W_{P20}/W_{F50}$  (where  $W_{F50}$  is the width as measured by our favored algorithm) is, on average,  $\sim 1.2$ , we replace the  $1.2W_{P20}$  term in Schneider *et al.* (1990) with  $1.4W_{F50}$ .  $\epsilon_S^{stat}$ , the statistical component of the integrated line flux error, is then given by

$$\epsilon_S^{stat} = 2 \text{ rms} \sqrt{1.4W_{F50}\Delta V} \quad (2)$$

(where *rms* is the r.m.s. figure, measured in the signal-free part of the spectral baseline and  $\Delta V$  is the velocity resolution of the spectrum). Our estimate of the total integrated line flux error,  $\epsilon_S$ , is then the sum in quadrature of the error contributions from statistical noise and baseline uncertainties, noise diode calibration, and correction coefficients. For the vast majority of the galaxies in the archive, this uncertainty is 10-15% of the corrected integrated flux  $S_c^{abs}$ .

### 3.2. Systemic Velocities and Velocity Widths

The systemic velocity of the HI line profile is usually derived as the midpoint of the segment that connects two points on opposite edges of the emission profile at a selected intensity level, usually some fraction of the mean or peak flux. The same algorithm is also used to derive the HI line width, and its extraction often dictates the choice of measurement algorithm. Over the years, numerous algorithms have been applied to derive width measures that both are robust in the presence of noise and most closely reflect the disk rotational velocity (Lewis 1983; Schneider *et al.* 1986; Chengalur *et al.* 1993). Algorithms applied originally to HI spectra contained in earlier datasets were optimized to produce consistent measurements in noisy spectra (e.g., Bicay & Giovanelli 1986) whereas more recent studies added emphasis on sampling the rotational velocity (Lavezzi & Dickey 1997).

The algorithm adopted to obtain HI line velocities and line widths here is very similar to that discussed by Chen-

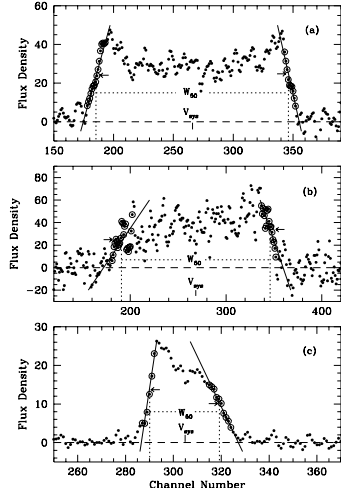


FIG. 2.— Examples of 21 cm line profiles, illustrating the systemic velocity and velocity width measuring algorithm. The spectral resolution and unit, in abscissa (“channel number”) is typically 2–11 km s<sup>-1</sup>. In panel (a), an average quality profile is illustrated, with horns near channel numbers 196 and 340 respectively. Straight lines are fit to the outer slopes of the profiles (circled points were used in the fit), and the channels corresponding to the flux level equal to 50% of the peak level, on the fit, are flagged. Velocities  $V_l$  and  $V_u$  defined in the text correspond, in panel (a), to the center of channels 185 and 347. Velocity width  $W_{50}$  (in spectrograph channel units) and systemic velocity are indicated. In panel (b), a low signal-to-noise profile is shown, illustrating some of the difficulties that can be encountered by the algorithm in identifying the horns and fitting the slopes. In panel (c), an asymmetric profile is shown, for which the identification of one of the horns is also arduous, due to the structural asymmetry of the line profile.

galur *et al.* (1993) and has been previously discussed in Haynes *et al.* (1999). Figure 2 illustrates the issues involved in systemic velocity and width extraction from global HI line profiles through simulations of representative cases. After identification of the flux level,  $f_p$ , of each of the spectral horns, the rising side of the profile is fit by a polynomial between the levels of 15% and 85% of  $f_p - rms$ . The velocity flagged for that side of the profile  $V_l$  is that for which the polynomial fit has a flux of 50% of the value of  $f_p - rms$ . This process is repeated for the other side of the profile to flag a velocity  $V_u$  at the corresponding level on the other horn. The adopted velocity width, hereafter designated  $W_{F50}$ , is defined as the difference between these two velocities  $W_{F50} = V_u - V_l$ , while the system velocity is their average  $V_{21} = (V_u + V_l)/2$ . In the vast majority of cases, the polynomial fits are straight lines. In rare cases, however, higher order fits are required and can be selected during the analysis stage.

This procedure has a major advantage over width algorithms which measure a width as the difference in velocities between points *on the spectrum itself* at N% of the peak flux. Under the scheme adopted here, noise effects on either side of the profile are averaged out. Additionally, the use of the parameter  $f_p - rms$  rather than simply  $f_p$  substantially reduces the dependence of the measured width on the signal-to-noise ratio (SNR). The most important flaws in the method are encountered when it is difficult to identify the location of the horns, such as

in low signal-to-noise profiles as shown in panel 2(b), or when one of the horns is missing as in the strongly asymmetric profile shown in panel 2(c) (see, e.g. Richter & Sancisi 1994 and Haynes *et al.* 1998). In these cases, the width measurement loses objectivity and accuracy and its derived error may not reflect the true uncertainty. For this reason, we also assign a width “quality index” to each result listed in Table 3.

To convert  $W_{F50}$  into a physical rotational velocity, four corrections must be applied: 1) an instrumental correction that accounts for the spectrometer resolution, smoothing applied to the spectrum, and SNR, 2) a cosmological redshift correction, 3) a correction for turbulent motions of the HI gas, and 4) a correction for the inclination of the disk to the line of sight. The widths presented here account for the first two effects only. The redshift correction is simply the instrumental-corrected width divided by a factor of  $1 + z$ , where  $z$  is the galaxy’s redshift. The instrumental correction is described in the following subsection. Although we do not apply such a correction, the effect of turbulent motions on the measurement of  $W_{F50}$  is discussed in Section 3.2.3.

In addition to the width measurement algorithm described above, each spectrum has been measured using four additional algorithms:  $W_{M50}$  is the width measured at 50% of the mean flux density,  $W_{P50}$  is the width measured at 50% of the value of the peak flux density minus the rms value  $f_p - rms$ ,  $W_{P20}$  is the width measured at 20% of the value of the peak flux density minus the rms value  $f_p - rms$ , and  $W_{2P50}$  is the width measured at 50% of each of the two peaks minus the rms value. We include these values to allow the interested reader to compare our width measurement results to those of other authors. However, we have derived corrections only for  $W_{F50}$ , not for any of the additional width measurements.

### 3.2.1. Smoothing

It is common practice to convolve radio spectra obtained with autocorrelation spectrometers with a one-channel-wide cosine function (in practice a [0.25,0.5,0.25] three-channel function: Hanning). This is done for two reasons. First, narrowband terrestrial interference, which occurs often within the observed spectral range even within parts of the spectrum protected by regulatory agreements for radio astronomical use, introduces “ringing” associated with the  $(\sin x)/x$  functional response of the spectrometer to single-channel-wide features. And, second, because of the finite number of correlator channels, the true autocorrelation function is truncated, resulting in its apparent multiplication by a rectangular function which is a multiple of the autocorrelation lag time; this in turn means that the true power spectrum has been convolved with the Fourier transform of this rectangular function, itself a “sinc function”. The application of Hanning smoothing reduces the spectral resolution of the observed spectrum. In some cases, further spectral smoothing is required by the low SNR of the observation or for other reasons; these measurements tend to be less useful for TF applications. All the HI spectra presented here are Hanning smoothed once (smoothing code H in our data tables, e.g. Haynes *et al.* 1997); in a minority of cases, as noted in our tabulations, three-channel “boxcar” averaging plus Hanning is applied instead (smoothing code B).

### 3.2.2. Instrumental and Noise Effects

Previous width measurement algorithms have often relied on measuring the width by computing the velocity difference between channels on either side of the profile. The channels are identified by either starting from inside the profile and searching outwards or starting outside and searching inwards, flagging the first channel to cross a flux limit that represents a particular fraction of the peak flux. This procedure creates a systematic bias in the width measurement as a function of the SNR (Lewis 1983). As described earlier, our width measurement procedure minimizes this effect by instead calculating the velocity difference between *polynomials that have been fit to several channels*. Nevertheless, there remains *some* dependence on the SNR, defined here as the ratio of the peak HI signal to the rms noise in the line-free portion of the spectrum, which we discuss in this section.

We have studied the instrumental and noise effect via simulations that incorporate autocorrelator spectrometer channel response and a variety of observed characteristics, such as profile slope and curvature. The simulations involve inputting a high resolution, noiseless profile, then binning the flux into channels, adding noise, and measuring the width of the profile using the same algorithm used also on the real data. This process is applied to a range of simulations adopting channel resolutions ranging from 5 to 11 km s<sup>-1</sup>, for the two different smoothing prescriptions, and for a variety of different profile shapes.

To account for the spectral noise, the true SNR of the spectrum can be characterized by  $\text{SNR} = (f_p - rms)/rms$ . The broadening of the width measurement is denoted by the parameter  $\lambda$ , which is one half the difference between the measured width and the width that would be measured in the absence of instrumental and noise effects (measured in channels). We can then account for the combined instrumental and noise effects by *subtracting an offset* from the measured width, parametrized as

$$\Delta s = 2\Delta v \lambda, \quad (3)$$

where  $\Delta v$  is the spectrometer channel separation in km s<sup>-1</sup> assumed to be equal to or very close to the channel width) and  $\lambda$  depends on the SNR and the type of smoothing.

The simulations suggest that  $\lambda$  is influenced by two competing effects. As our width measurement algorithm measures a best-fit line to the sides of the profile at 50% of the value of  $f_p - rms$ , the two parameters in play are 1) the value of  $f_p - rms$ , and 2) the range of spectral values over which the line is fit.

If instrumental and noise effects increase (decrease)  $f_p - rms$ , then  $\lambda$  will decrease (increase), as a higher (lower) 50% value corresponds to a narrower (broader) width. Even in the absence of noise, the peak flux is depressed by channel binning and smoothing, broadening the measured width. For realistic values of SNR, however, the situation is more complicated. One can characterize  $f_p - rms$  with the expression

$$f_p - rms = \text{Max}(y_i + \delta_i rms) - rms, \quad (4)$$

where  $y_i$  is the flux of channel  $i$  that one would measure in the absence of noise and  $\delta_i$  is a gaussian random variable describing the noise contribution to channel  $i$ . We

find that profiles with steep inner slopes observed with broad channel spacings tend to produce decreasing values of  $f_p - rms$  with increasing  $rms$ . Other profile shapes and spectral resolutions give a somewhat more complicated dependence. So the variation of  $f_p - rms$  affects the profile width measurement, but whether it becomes broader or narrower depends on the details of the profile shape and resolution.

$\lambda$  is also influenced by the range over which the line is fit to the sides of the profile. The endpoints of the fit are found by searching outward from each peak, identifying the first channels with flux less than 15% and 85% of  $f_p - rms$ . This method introduces a slight bias towards the inclusion of channels whose flux has been *depressed* by noise. For noisier profiles, the region over which the line is fit also moves closer to the peak of the profile, where the slope is shallower. Both of these effects preferentially select channels with flux that falls *below* the best fit line in the noiseless case, leading to narrower width measurements. This effect dominates the dependence of  $\lambda$  on SNR over the range  $0.6 < \log(\text{SNR}) < 1.1$  for each of our channel resolutions and for all realistic profile shapes, meaning that  $\lambda$  increases with SNR over that range.

The simulations show that the most relevant line profile parameters in determining  $\lambda$  are the slopes on each side of each of the two peaks and the number of channels leading up to the peaks. While  $\lambda$  typically varies by  $\sim 0.5$  channels for the same profile shape with different values of the SNR, the variation can be even greater ( $\sim 1$  channel) among different profile shapes *and* among different noise realizations of the same profile for constant SNR, channel width, and smoothing prescription. This variation limits our ability to determine  $\lambda$  precisely for a real profile. However, we can simply apply our simulation results for a profile with mid-range values for the inner and outer slopes and number of channels leading up to the peaks. The resulting approximate solution gives:

$$\lambda = \lambda_1(\Delta v) \quad \text{for } \log(\text{SNR}) < 0.6 \quad (5)$$

$$\lambda = \lambda_2(\Delta v) + \lambda'_2(\Delta v)\log(\text{SNR}) \quad \text{for } 0.6 < \log(\text{SNR}) < 1.1 \quad (6)$$

$$\lambda = \lambda_3(\Delta v) \quad \text{for } \log(\text{SNR}) > 1.1 \quad (7)$$

The values of  $\lambda_1(\Delta v)$ ,  $\lambda_2(\Delta v)$ ,  $\lambda'_2(\Delta v)$ , and  $\lambda_3(\Delta v)$  are constants for both  $\Delta v < 5$  km s<sup>-1</sup> and  $\Delta v > 11$  km s<sup>-1</sup>, but depend linearly on  $\Delta v$  within the range  $5 < \Delta v < 11$  km s<sup>-1</sup>. The values of these parameters for each of the channel widths and smoothing prescriptions can be found in Table 2. We stress that both the linear dependence of  $\lambda$  on  $\log(\text{SNR})$  in the range  $0.6 < \log(\text{SNR}) < 1.1$  and the linear dependence of the  $\lambda_i$ 's on  $(\Delta v)$  in the range  $5 < \Delta v < 11$  km s<sup>-1</sup> are approximate and completely empirical. We also keep the  $\lambda_i$ 's constant outside the range  $5 < \Delta v < 11$  km s<sup>-1</sup> solely because few of our observations have channel resolutions far outside of that range, and we have done little testing of the width corrections outside that range.

In addition to the instrumental and smoothing corrections, the observed width must also be corrected for redshift stretch, giving:

$$W_c = (W_{F50} - \Delta_s)/(1+z) = (W_{F50} - 2\Delta v \lambda)/(1+z) \quad (8)$$

TABLE 2  
VELOCITY WIDTH INSTRUMENTAL CORRECTION PARAMETERS

$\Delta v$	<i>smoothing</i>	$\lambda_1(\Delta v)$	$\lambda_2(\Delta v)$	$\lambda'_2(\Delta v)$	$\lambda_3(\Delta v)$
$< 5 \text{ km s}^{-1}$	H	0.005	-0.4685	0.785	0.395
$5\text{-}11 \text{ km s}^{-1}$	H	$0.037\Delta v - 0.18$	$0.0527\Delta v - 0.732$	$-0.027\Delta v + 0.92$	$0.023\Delta v + 0.28$
$> 11 \text{ km s}^{-1}$	H	0.227	-0.1523	0.623	0.533
$< 5 \text{ km s}^{-1}$	B	0.020	-0.4705	0.820	0.430
$5\text{-}11 \text{ km s}^{-1}$	B	$0.052\Delta v - 0.24$	$0.0397\Delta v - 0.669$	$0.020\Delta v + 0.72$	$0.062\Delta v - 0.12$
$> 11 \text{ km s}^{-1}$	B	0.332	-0.2323	0.940	0.802

### 3.2.3. Turbulent Motion Correction

The HI clouds in a disk do not move along strictly circular orbits. Even in the absence of large-scale anomalies, such as warps, bars and other global asymmetries, deviations from circular motion occur, such as those associated with small-scale dispersion and streaming motions near spiral arms. Bottinelli *et al.* (1983) have suggested that the contribution to the observed width of turbulent motions, or otherwise small-scale deviations from circular rotation, could be expressed via a term  $W_t$ , additive to the circular width in the form:  $W = 2V_{max} \sin i + W_t$  where  $i$  is the disk inclination and  $V_{max}$  the maximum rotational width. Tully & Fouqué (1985) found that, while a linear correction to the observed width may well account for the effect of turbulent motions on large widths, for low luminosity galaxies a quadratic combination would be more appropriate (see also Fouqué *et al.* 1990a). They thus proposed a formula, their Equation 12, that yields a linear combination at large widths, a quadratic combination at small widths, and a transitional form at intermediate widths. This formula was adopted by a variety of other authors (e.g., Broeils 1992; Rhee 1996; Verheijen 1997) who also measure HI widths at N% of the profile peak. These authors measure the value of the  $W_t$  parameter by minimizing the scatter between the turbulence-corrected velocity widths and the velocity widths determined from rotation curves of the same galaxies. Verheijen (1997) reviews the results of the aforementioned authors, and notes that the optimal value of  $W_t$  strongly depends on the instrumental correction used.

Since we do not measure velocity widths at N% of the profile peak, and our instrumental correction differs from that of these other authors, we are not justified in adopting any of the previous values of  $W_t$ . Instead, we derive our own turbulent motion correction by introducing a random, isotropic  $\sigma = 10 \text{ km s}^{-1}$  turbulent motion into the simulations described in the previous subsection. We find that this depresses the peak flux, and thus broadens the measured profile width by moving the 50% value farther from the profile center. As in Verheijen (1997) and references therein, the amount of turbulence-induced width broadening is found to vary greatly from galaxy to galaxy, depending on the details of the profile shape. We do not find a discernable trend in the amount of width broadening with profile width or signal-to-noise ratio. For the sake of simplicity, we thus subtract the turbulence correction from the width linearly, with the equation:  $W_{c,t} = W_c + W_t$ , where  $W_t = 6.5 \text{ km s}^{-1}$ . Lavezzi & Dickey (1997) likewise discuss the merits of a

simple linear subtraction of a turbulence term.

As stated earlier, in order to use  $W_c$  for applications such as those involving the Tully-Fisher relation, corrections for both inclination angle and turbulence must be applied as well. Because of its uncertainty, the values of corrected width  $W_c$  reported here *do not include that correction*, nor is viewing angle considered. Authors wishing to make full use of the data should apply those corrections themselves.

## 4. DATA COMPILATION

All of the spectra in the archive have been newly reprocessed using the new flux and width corrections. The spectra themselves will be made available through the U.S. National Virtual Observatory. Here, we provide the corrected and uncorrected spectral parameters. In Table 3, we present the results for all 8852 spectra for which we are confident that we have detections. The format, described below, closely resembles that of Haynes *et al.* (1999) Table 1:

Column (1). Entry number in the UGC, where applicable, or else in our private database, referred to as the Arecibo General Catalog (AGC).

Column (2). NGC or IC designation, or other name, typically from the *Catalog of Galaxies and Clusters of Galaxies* (Zwicky *et al.* 1961-1968), ESO, or the *Morphological Catalog of Galaxies* (Vorontsov-Velyaminov & Arhipova 1968). Where used, the designation in the latter is abbreviated to eight characters.

Columns (3) and (4). Right Ascension and Declination in the J2000.0 epoch either from the NASA/IPAC Extragalactic Database (NED)<sup>6</sup> or measured by us on the POSS-I. Typically, the listed positions have  $\leq 5''$  accuracy.

Column (5). The blue major and minor diameters,  $a \times b$ , in arcminutes, either from the UGC or ESO catalogs or as estimated by us on the POSS-I.

Column (6). The morphological type code following the RC3 system. Classification comes either from the UGC or ESO catalogs or from our own visual examination of the POSS-I prints.

Column (7). The observed integrated 21 cm HI line flux  $S_{obs} = \int S dV$  in  $\text{Jy km s}^{-1}$ .

Column (8). The corrected integrated 21 cm HI line flux  $S_c$ , also in  $\text{Jy km s}^{-1}$ , after corrections applied for pointing offsets (Arecibo line/flat feed spectra only) and

<sup>6</sup> The NASA/IPAC Extragalactic Database is operated by the Jet Propulsion Laboratory, California Institute of Technology, under contract with the National Aeronautics and Space Administration.

source extent following Section 3.1.

Column (9). The self-absorption corrected integrated 21 cm HI line flux  $S_c^{abs}$ , also in  $\text{Jy km s}^{-1}$ , after corrections applied for pointing offsets (Arecibo line/flat feed spectra only), source extent, and HI self-absorption, following Section 3.1.

Column (10). The uncertainty  $\epsilon_S$  in the self-absorption corrected integrated flux  $S_c^{abs}$ , following Section 3.1.1.

Column (11). The rms noise per channel of the spectrum, rms, in mJy.

Column (12). The emission profile signal-to-noise ratio, SNR, taken as the ratio of the peak HI line flux to the rms noise within the signal-free portion of the spectrum. Unlike in Section 3.2.2, we do not subtract the rms from the peak flux before dividing by the rms.

Column (13). The heliocentric velocity  $V_\odot$ , in  $\text{km s}^{-1}$ , of the HI line signal, taken as the midpoint of the profile at the 50% level also used to measure the width (see below).

Column (14-18). The full velocity width of the HI line in  $\text{km s}^{-1}$ , uncorrected for redshift or other effects, using the five measurement algorithms discussed in Section 2.2. Widths are  $W_{F50}$ ,  $W_{M50}$ ,  $W_{P50}$ ,  $W_{P20}$ , and  $W_{2P50}$  respectively.

Column (19). A corrected velocity width  $W_c$ , in  $\text{km s}^{-1}$ , which accounts for redshift stretch, instrumental effects, and smoothing. The correction is applied to  $W_{F50}$ . Note that this width is not rectified for viewing angle or turbulence.

Column (20). The estimated error on  $W_c$ ,  $\epsilon_w$ , in  $\text{km s}^{-1}$ , taken to be the sum in quadrature of the measurement error and the estimated error in broadening corrections. The estimated error on the velocity itself,  $\epsilon_V$ , can be approximated as  $\epsilon_w/2^{1/2}$ .

Column (21). A code indicating the instrument used: (AOlf) Arecibo, line feed system; (AOff) Arecibo, flat feed system; (AOG) Arecibo Gregorian; (Efs) Effelsberg 100 m; (GB300) Green Bank 91 m; (GB140) Green Bank 42 m; (Nanc) Nancay.

Column (22). Bandwidth of the spectrum in kHz  $\Delta f$ .

Column (23). Number of channels in the spectrum  $N_{chan}$ .

Column (24). Three codes indicating the smoothing, width quality, and inclusion in the 2001 Arecibo observations.

The first code is the smoothing code: (H) single Hanning only; (B) Hanning plus three-channel boxcar.

The second is a qualitative assessment of the quality of the profile: (G) good; (F) fair; (S) single peak; (P) poor quality for TF applications; (C) confused; (A) shows absorption. Velocity widths measured from profiles classified as good detections should be useful for TF applications; those measured on profiles denoted ‘‘F’’ should be used with caution. Because the width measuring algorithm is designed for application to two-horned profiles, the widths measured on single peaked profiles should also be used with caution, as they may underestimate the true rotation width. Widths in the last two categories cannot be used for TF purposes. Confusion is identified only when contamination from another galaxy in the beam is certain.

The third code where applicable indicates, with a ‘‘\*’’, inclusion in the sample observed with the Arecibo Tele-

scope in the fall of 2001 as described in Section 2.2.

In addition to the HI detections presented in Table 3, Tables 4 and 5 also summarize useful data about objects for which homogeneous upper limits to the HI flux can be calculated. Table 4 contains summary data for 156 galaxies classified as ‘‘marginal’’ detections, that is, for those cases in which the signal has not been verified through adequate reobservation. Table columns match those of Table 3, except that we omit Columns 14-20 because of their uncertainty, and Column 24 because, in this instance, all spectra have been both Hanning and Boxcar smoothed. Table 4 also adds Column 25, the heliocentric velocity as derived from optical observations,  $V_{\odot-opt}$ , in  $\text{km s}^{-1}$ , taken from the NED. Although the parameters extracted from the HI line profile are uncertain, the coincidence of the HI signal with the expected location in frequency corresponding to the optical redshift brings a measure of believability to the possible HI signal. Such objects may be deserving of further, deeper HI observations which probe sensitivities significantly greater than those presented here.

In Table 5, we present summary results for objects which are classified as the HI line nondetections, except that Columns 7, 8, 9, 10, 12, and 13 are also omitted. Column 26 adds the heliocentric velocity  $V_{cent}$  corresponding to the central frequency of the band searched for HI emission. Only objects for which the radio frequency band covered by the spectrum included the frequency expected from the optical redshift are listed in this table. Upper limits to the HI line flux can be estimated from the rms noise per channel and an assumption of the HI profile shape. A simple estimate of the upper limit to the integrated HI line flux, useful for calculating an upper limit to the HI mass for non-detections, adopts a rectangular profile of height  $1.5 \text{ rms } \delta W$ , where  $\delta W$  is the full width of the Doppler broadened HI line, expected, for example, for a galaxy of a given optical luminosity given by the Tully-Fisher relation.

## 5. DATASET CHARACTERISTICS AND LIMITATIONS

In contrast to a wide area, HI blind survey like HIPASS, the archival dataset presented here is extremely heterogenous in terms of its sky coverage, depth and completeness. At the same time, it contains HI line spectra for more than twice as many detections as the HIPASS HICAT (Meyer *et al.* 2004), with much higher typical sensitivity and probing a greater volume.

The sky distribution for all detected galaxies listed in Table 3 is shown in Figure 3. The unevenness of sky coverage, with strong preference for that portion of the sky visible to the Arecibo telescope, is clearly evident. In fact, 77 % of the objects fall within the Arecibo declination limits ( $-2^\circ < \text{Dec.} < +38^\circ$ ). The southern cutoff at  $\text{Dec.} \sim -40^\circ$  represents the limitations of the steerable northern hemisphere telescopes that were used. There is also a strong deficiency of objects in the Zone of Avoidance, not just because the archive is comprised of objects with known optical counterparts but also because several of the previous surveys have avoided regions of high galactic extinction for reasons of photometric accuracy and completeness at optical wavelengths.

The sky distribution of targeted galaxies also reflects the large scale structure within the survey volume, evident both in Figure 3 and in the redshift distribution

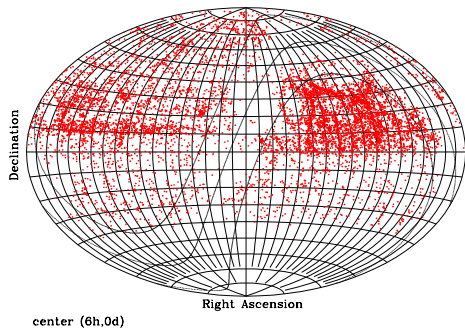


FIG. 3.— Aitoff equal area projection of the sky distribution of galaxies in the HI archive. Shown here are all galaxies with reliable HI fluxes and widths (all those listed in Table 3). The plot is centered at R.A. =  $6^h$ . The thick lines trace the galactic latitudes  $b = -20^\circ$ ,  $b = 0^\circ$ , and  $b = +20^\circ$ .

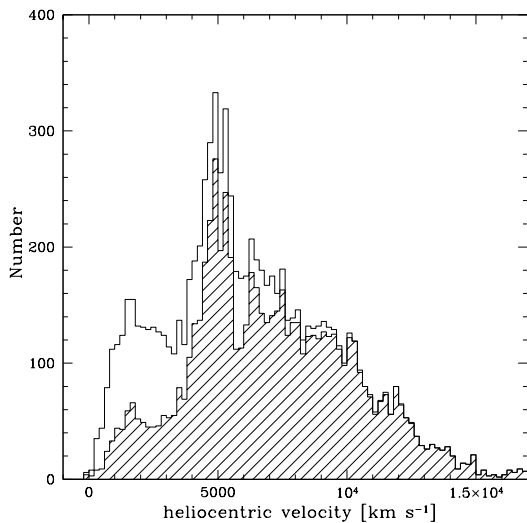


FIG. 4.— Distribution of heliocentric radial velocities for all galaxies in the archive, in bins of width  $200 \text{ km s}^{-1}$ . Observations conducted at Arecibo are indicated by the shaded histogram. The impact of local large scale structures and the preferential coverage corresponding to that part of the celestial sphere visible to the Arecibo telescope, is evident.

illustrated in Figure 4. The most prominent feature is the Pisces-Perseus Supercluster at  $22^h < \text{R.A.} < 4^h$  and  $cz \sim 5000 \text{ km s}^{-1}$  which has been the target of several past observing programs. Also seen clearly is the Virgo region toward the center of the Local Supercluster at R.A.  $\sim 12^h$ ,  $cz \sim 1500 \text{ km s}^{-1}$ .

The distributions of the rms noise per channel and SNR are shown in Figures 5 and 6 respectively. Because of the superior gain and angular resolution of the Arecibo telescope, observations undertaken with it are typically more sensitive than ones conducted with other instruments. For this reason, the fraction of the archival dataset ex-

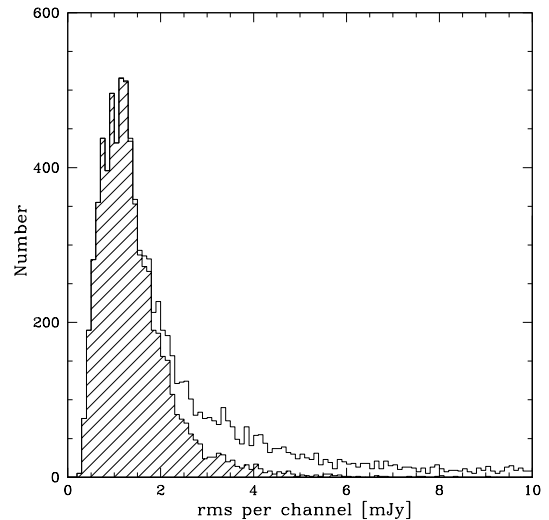


FIG. 5.— Distribution of rms noise values per channel for all galaxies in the archive, in bins of width  $0.1 \text{ mJy}$ . Observations conducted at Arecibo are indicated by the shaded histogram.

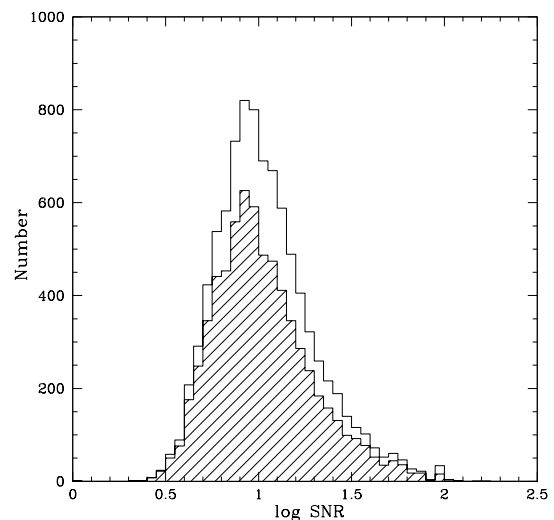


FIG. 6.— Distribution of peak-signal-to-rms noise ratios, SNR, for all galaxies in the archive, in bins of width  $0.05 \text{ dex}$ . Observations conducted at Arecibo are indicated by the shaded histogram.

tracted from Arecibo observations is indicated separately in those figures. The diversity of the observational programs which have contributed datasets to this HI archive is evident in these distributions. In some instances, the targetting of objects for the explicit purpose of measuring comparative HI content or accurate HI line widths has placed more stringent demands for lower rms noise values, or higher SNR, than, for example, those programs that were conducted principally as wide area redshift surveys.

The total integrated (corrected) and peak HI line flux distributions are shown in Figure 7 and 8 respectively. Comparing these figures to the corresponding distributions for the HIPASS/HICAT blind HI survey shown in Figure 9 of Meyer *et al.* (2004) and Figure 4 of Zwaan *et al.* (2004), it is readily apparent that the optically-

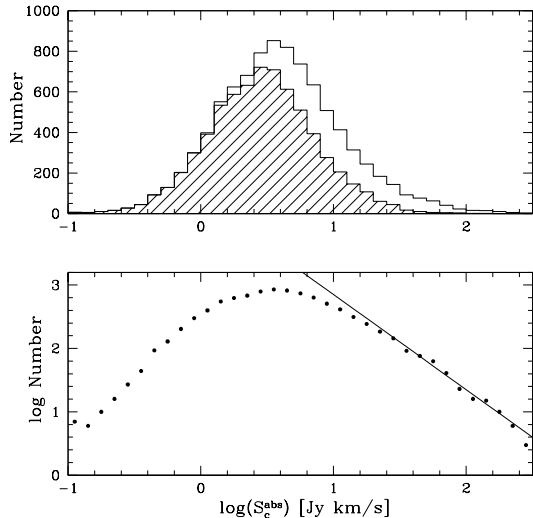


FIG. 7.— Distribution of corrected HI fluxes  $S_c^{abs}$  for all galaxies in the archive, in bins of width 0.1 dex. Observations conducted at Arecibo are indicated by the shaded histogram. The solid line in the *bottom* plot traces the case where  $\log N_{galaxies} \propto -1.5 \log S_c^{abs}$ , which is the dependence expected of an HI flux limited sample.

targeted archive presented here contains a substantial number of galaxies with both integrated fluxes and peak fluxes well below those included in the HIPASS catalog. The HICAT sample contains very few objects with  $S_{HI} < 2.5 \text{ Jy km s}^{-1}$ , whereas almost one third of the optically selected sample presented here have fluxes  $S_c^{abs}$  lower than that value. Likewise, HICAT strives to be peak flux limited and contains almost no sources with peak HI fluxes below 30 mJy, whereas the majority of galaxies in the optically-selected sample have peak fluxes below that value.

For an HI flux limited sample, the logarithm of the number of galaxies per unit  $\log S_c^{abs}$  should be proportional to  $-1.5 \log S_c^{abs}$ ; this relationship should also hold for the peak flux in a peak flux limited sample. The bottom panels of Figures 7 and 8 show the log-log distributions of corrected flux  $S_c^{abs}$  and peak HI line flux  $S_{peak}$ , with the  $N \propto -1.5 \log S$  line superposed for reference. Clearly the optically-selected sample is neither peak HI flux nor total HI flux limited as the HI-blind surveys strive to be. However, as shown in Springob, Haynes, & Giovanelli (2005), with the addition of supplemental data from the literature, it is possible to extract an optical diameter limited and HI flux limited subsample, restricted to the portion of the sky lying within the Arecibo declination limits.

Figure 9 shows the distribution of instrumentally-corrected (but not turbulence- or inclination-corrected) widths  $W_c$  for all galaxies in the archive. Objects with confused, asymmetric or otherwise oddly behaved spectral profiles (coded “C”, “P” or “F” in Table 3) are included in the full distribution, but profiles which are classified as “G” or “S” are included in the shaded area. In comparison to the HIPASS/HICAT dataset, the galaxies included in this optically-selected sample are preferentially faster rotators, unsurprising given the Tully-

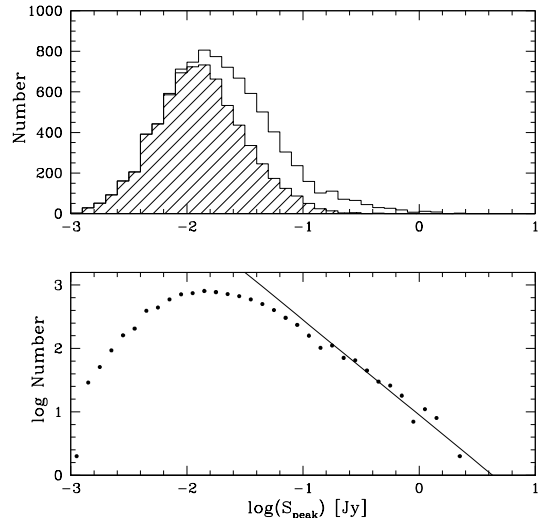


FIG. 8.— Distribution of peak HI fluxes  $S_{peak}$  for all galaxies in the archive, in bins of width 0.1 dex. Observations conducted at Arecibo are indicated by the shaded histogram. The solid line in the *bottom* plot traces the case of  $\log N_{galaxies} \propto -1.5 \log S_{peak}$ , which is the dependence expected of a peak flux limited sample. The heterogeneous nature of the observations that contribute to this sample is very evident by the lack of a cutoff minimum  $S_{peak}$ .

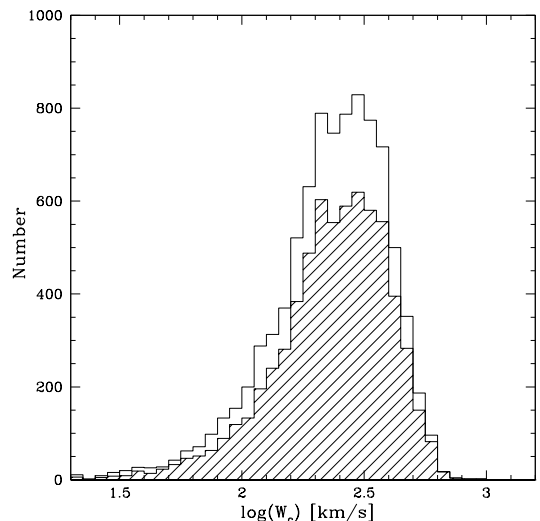


FIG. 9.— Distribution of corrected HI widths  $W_c$  for all galaxies in the archive except those identified as confused, in bins of width 0.05 dex. Observations conducted at Arecibo are indicated by the shaded histogram.

Fisher relation and the much larger volume sampled here. This dataset is being used to derive the observationally-based rotational velocity function for HI disk systems (Springob, Haynes & Giovanelli, in preparation).

There is one interesting issue for which much of this dataset is unfortunately largely unsuited: the study of global asymmetry in HI profiles (Richter & Sancisi 1994; Haynes *et al.* 1998). As discussed in Section 3.1, the shapes of global HI profiles observed with single dish telescopes are affected by both beam attenuation and pointing offsets and errors. Prior to its recent upgrade, the Arecibo telescope L-band feeds were subject to point-

ing errors of typically 20–30'' but sometimes larger, especially when the observations were conducted at large zenith angle. We therefore caution against using the spectra contained in the AGC digital archive for studies of asymmetry, with the exception of the very carefully collected Green Bank 42 m telescope dataset obtained for that very purpose as discussed in Haynes *et al.* (1998).

## 6. SUMMARY

We present here a compilation of HI spectral parameters for more than 9000 optically-targeted galaxies in the local universe which have been observed by us and our collaborators over the last 20+ years. All of the HI spectra have been reprocessed in a homogenous manner and a single set of algorithms has been used to extract spectral parameters which can then be corrected to physical parameters taking into account the instrument- and processing-related complications such as spectral resolution, source extent, pointing offsets and signal-to-noise. We use both empirical evidence and the results of simulated observations to produce recipes for deriving these physical parameters from the observed ones based on all of the information available from the digital spectra themselves.

The recent blind HI surveys such as HIPASS offer the advantage of completeness and homogenous data processing and parameter extraction. By reprocessing all of our existing HI line spectra using software specifically designed to exploit the details of the observing set-ups and the characteristics of the spectra themselves, we have tried to minimize the effects of instrument- and processing-related differences among the datasets. At the same time, HI completeness issues remain in optically targeted samples, despite their greater depth and sensitivity. It is well known that optical galaxy catalogs often preferentially miss the low optical surface brightness but HI-rich late type galaxies that are common in the local universe. In contrast, blind HI surveys do not suffer from this strong bias (Rosenberg & Schneider 2002; Koribalski *et al.* 2004). A more thorough discussion of the completeness of the AGC HI compilation in the context of the derivation of the HI mass function is presented in Springob, Haynes & Giovanelli (2005). Despite the lack of flux completeness, the redshift, emission line flux, and observed rotational widths available from the global HI

line profiles collected here provide important measures of fundamental galaxy properties useful to diverse studies of galaxies in the nearby universe, especially when combined with complementary multiwavelength data.

In addition to the tabulations contained herein, the actual smoothed and baseline subtracted spectra are available in digital form by contacting the authors. Plans are underway to make the entire dataset available through the US National Virtual Observatory in conjunction with a wide area blind HI survey to be undertaken at Arecibo beginning in 2005. This *Arecibo Legacy Fast ALFA* (ALFALFA) survey will make use of the new 7-feed dual polarization, L-band array (ALFA) to survey over 7000 deg<sup>2</sup> of the sky visible to Arecibo, detecting tens of thousands of HI sources, from local, very low HI mass dwarfs to gas-rich massive galaxies seen to  $z \sim 0.06$ . A careful study of the detection statistics of the present optically selected sample in such a sensitive HI blind survey will provide insight into the differential characteristics of galaxies according to optical surface brightness and HI content. Only the mining of datasets derived from wide area surveys conducted at multiple wavelengths will, in combination, provide the true census of all galaxies that occupy the local universe.

We wish to thank our numerous collaborators, colleagues, students, telescope staff and friends who have participated over many years and in many places and contexts in the acquisition of the original data used to produce this archive. We especially thank Barbara Catinella for conducting the fall 2001 Arecibo observations, and Joe McMullin, Bob Garwood, Karen O'Neil, and Jeremy Darling for their work in adapting AIPS++ for use with Arecibo spectral line data. This work has been partially supported by AST-9900695, AST-0307396, AST-0307661, the N.R.A.O./GBT 03B-007 Graduate Student Support Grant and the NASA New York State Space Grant.

**Tables 3, 4, and 5** (in ASCII format) are exclusively available online at <http://egg.astro.cornell.edu/hiarchive/hiarchive.html>.

## REFERENCES

- Barnes, D.G., Staveley-Smith, L., de Blok, W.J.G., Oosterloo, T. Stewart, I.M. *et al.* 2001, MNRAS, 322, 486  
 Bicay, M.D. & Giovanelli, R. 1986, AJ, 91, 705  
 Botinelli, L., Gouguenheim, L., Paturel, G., & de Vaucouleurs, G. 1983, A&A, 118, 4  
 Braun, R. 1997, ApJ, 484, 637  
 Bridle, A.H., Davis, M.M., Fomalont, E.B., & Lequeux, J. 1972, AJ, 77, 405  
 Broeils, A. 1992, Ph.D. Thesis, Univ. of Groningen  
 Chengalur, J.N., Salpeter, E.E., & Terzian, Y. 1993, ApJ, 419, 30.  
 de Vaucouleurs, G., de Vaucouleurs, A., Corwin, H.G., Buta, R.J., Paturel, G., & Fouqué, P. 1991, Third Reference Catalogue of Bright Galaxies (New York: Springer)(RC3)  
 Fouqué, P., Bottinelli, L., Gouguenheim, L., & Patruel, G. 1990a, ApJ, 349, 1  
 Fouqué, P., Durand, N., Bottinelli, L., Gouguenheim, L., & Patruel, G. 1990b, A&AS, 86, 473  
 Freudling, W., Haynes, M.P. & Giovanelli, R. 1988, AJ, 97, 1791  
 Freudling, W., Haynes, M.P. & Giovanelli, R. 1992, ApJS, 79, 157  
 Giovanelli, R. & Haynes, M.P. 1989, AJ, 97, 633  
 Giovanelli, R. & Haynes, M.P. 1993, AJ, 105, 1271  
 Giovanelli, R., Haynes, M.P., Myers, S.R. & Roth, J. 1986, AJ, 92, 250.  
 Giovanelli, R., Haynes, M.P., Salzer, J.J., Wegner, G., da Costa, L.N., and Freudling, W. 1994, AJ, 107, 2036  
 Giovanelli, R., Avera, E. & Karachentsev, I.D. 1997, AJ, 114, 122  
 Haynes, M.P. & Giovanelli, R. 1984, AJ, 89, 758 (HG84)  
 Haynes, M.P. & Giovanelli, R. 1986, ApJ, 306, 466  
 Haynes, M.P. & Giovanelli, R. 1991a, AJ, 102, 841  
 Haynes, M.P. & Giovanelli, R. 1991b, ApJS, 77, 331  
 Haynes, M.P., Magri, C., Giovanelli, R. & Starosta, B.M. 1988, AJ, 95, 607  
 Haynes, M.P., Giovanelli, R., Herter, T., Vogt, N.P., Freudling, W., Maia, M., Salzer, J.J. & Wegner, G. 1997, AJ, 113, 1197  
 Haynes, M.P., van Zee, L., Hogg, D.E., Roberts, M.S., & Maddalena, R.J. 1998, AJ, 115, 62  
 Haynes, M.P., Giovanelli, R., Chamaraux, P., Freudling, W., da Costa, L.N., Salzer, J.J. & Wegner, G. 1999, AJ, 117, 2039  
 Hewitt, J.N., Haynes, M.P., & Giovanelli, R. 1983, AJ, 88, 272 (HHG)

- Huchtmeier, W.K. & Richter, O.-G. 1989, A General Catalog of HI Observations of Galaxies. The reference catalog (Berlin, Heidelberg, New York: Springer-Verlag)
- Kilborn, V.A., Staveley-Smith, L., Marquarding, M., Webster, R.L., Malin, D.F. *et al.* 2000 AJ, 120, 1342
- Koribalski, B.S., Staveley-Smith, L., Kilborn, V.S., Ryder, S.D., Kraan-Korteweg, R.C. *et al.* 2004, AJ, 128, 16.
- Lang, R.H., Boyce, P.J., Kilborn, V.A., Minchin, R.F., Disney, M.J. *et al.* 2003, MNRAS, 342, 738
- Lauberts, A. 1982, ESO-Uppsala Survey of the ESO(B) Atlas (Munich: ESO)(ESO)
- Lavezzi, T.E. & Dickey, J.M. 1997, AJ, 114, 2437
- Lewis, B.M. 1983, AJ, 88, 962
- Magri, C. 1994, AJ, 108, 896
- Magri, C., Haynes, M.P., Forman, W., Jones, C. & Giovanelli, R. 1988, ApJ, 333, 136
- Meyer, M.J. *et al.* 2004, MNRAS, 350, 1195
- Nilson, P. 1973, Uppsala General Catalog of Galaxies (Uppsala: Astr. Obs. Pub.)(UGC)
- Rhee, M.-H. 1996, Ph.D. Thesis, Univ. of Groningen
- Richter, O.-G. & Sancisi, R. 1994, A&A, 290, 9
- Rosenberg, J.L. & Schneider, S.E. 2000, ApJS, 130, 177
- Rosenberg, J.L. & Schneider, S.E. 2002, ApJ, 567, 247
- Schneider, S.E., Helou, G., Salpeter, E.E. & Terzian, Y. 1986, AJ, 92, 742
- Schneider, S.E., Thuan, T.X., Magri, C., & Wadiak, J.E., 1990, ApJS, 72, 245
- Scodreggio, M., Solanes, J.M., Giovanelli, R., & Haynes, M.P. 1995, ApJ, 444, 41
- Shostak, G.S. 1978, A&A, 68, 321
- Springob, C.M., Haynes, M.P. & Giovanelli, R. 2005, ApJ, 621, 215
- Tully, R.B. & Fisher, J.R. 1977, A&A, 54, 661
- Tully, R.B. & Fouqué, P. 1985, ApJS, 58, 67
- van Zee, L., Haynes, M.P. & Giovanelli, R. 1995, AJ, 109, 990
- van Zee, L., Maddalena, R.J., Haynes, M.P., Hogg, D.E., & Roberts, M.S. 1997, AJ, 113, 1638
- Verheijen, M.A.W. 1997, Ph.D. Thesis, Univ. of Groningen
- Vorontsov-Velyaminov, B.A. & Arhipova, V.P. 1968, Morphological Catalog of Galaxies (Moscow: Moscow State Univ.)
- Wegner, G., Haynes, M.P. & Giovanelli, R. 1993, AJ, 105, 1251
- Zwaan, M.A., Briggs, F.H., Sprayberry, D., & Sorar, E. 1997, ApJ, 490, 173
- Zwaan, M.A., Meyer, M.J., Webster, R.L., Staveley-Smith, L., Drinkwater, M.J. *et al.* 2004, MNRAS, 350, 1210
- Zwicky, F., Herzog, E., Wild, P., Karpowicz, M., & Kowal, C. 1961-1968, Catalog of Galaxies and Clusters of Galaxies (Pasadena: California Inst. of Tech. Press)